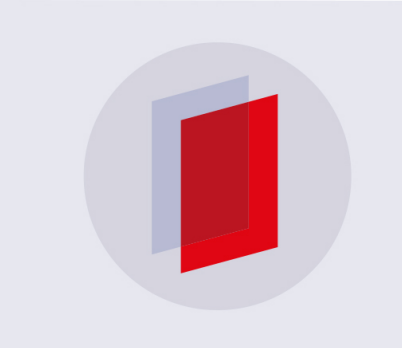
PAPER

Angular-dependent interatomic potential for the binary Ni-Cr system

To cite this article: C A Howells and Y Mishin 2018 Modelling Simul. Mater. Sci. Eng. 26 085008

View the article online for updates and enhancements.



IOP ebooks™

Bringing you innovative digital publishing with leading voices to create your essential collection of books in STEM research.

Start exploring the collection - download the first chapter of every title for free.

Angular-dependent interatomic potential for the binary Ni–Cr system

C A Howells and Y Mishin®

Department of Physics and Astronomy, MSN 3F3 George Mason University, 4400 University Drive, Fairfax, VA 22030-4444, United States of America

E-mail: chowells@gmu.edu and ymishin@gmu.edu

Received 8 July 2018, revised 16 September 2018 Accepted for publication 25 September 2018 Published 29 October 2018



Abstract

A new interatomic potential has been developed for the Ni–Cr system in the angular-dependent potential (ADP) format by fitting the potential parameters to a set of experimental and first-principles data. The ADP potential reproduces a wide range of properties of both elements as well as binary alloys with reasonable accuracy, including thermal and mechanical properties, defects, melting points of Ni and Cr, and the Ni–Cr phase diagram. The potential can be used for atomistic simulations of solidification, mechanical behavior and microstructure of the Ni-based and Cr-based phases as well as two-phase alloys.

Keywords: atomistic modeling, interatomic potential, Ni-Cr system, phase diagram

(Some figures may appear in colour only in the online journal)

1. Introduction

Nickel-chromium alloys present significant interest for automotive, aerospace, nuclear and other technological applications. For example, Ni and Cr are the basic chemical components of the industrial Inconel alloys, which additionally contain Fe, Mo, Nb and other alloying elements. Inconels demonstrate an attractive combination of high-temperature strength and excellent oxidation resistance, which makes them ideal for service in extreme environments. The binary Ni–Cr system is a convenient model of Inconels suitable for basic studies. The Ni–Cr phase diagram contains solid solutions based on the face-centered cubic (fcc) Ni and body-centered cubic (bcc) Cr, which are separated by a miscibility gap and melt by a eutectic reaction [1, 2].

Atomistic computer simulations are capable of providing atomic-level insights and predicting numerical values of properties that cannot be readily measured experimentally. The accuracy of the results depends on the accuracy and reliability of the interatomic potentials

employed in the simulations. While several good-quality potentials have been developed for Ni [3–5], Cr has received much less attention. Two embedded-atom method (EAM) potentials [6, 7] and a modified EAM potential [8] for Cr can be found in the literature. These potentials have not been extensively tested for key properties of Cr, such as the energies of alternate crystal structures, surface energies, thermal expansion, phonon dispersion relations, melting temperature, and others that are most important for atomistic simulations. Likewise, the existing EAM potential for the binary Ni–Cr system only exists as part of a ternary Fe–Ni–Cr [9] and quaternary Fe–Ni–Cr–Pd [10] potentials. The latter was constructed and tested focusing on radiation defects and diffusion in the fcc-based solid solution under service conditions in nuclear reactors.

In this paper we propose a new interatomic potential for the Ni–Cr system. Considering that Cr is a bcc metal with a partially filled d-band, we choose the angular-dependent potential (ADP) format [3, 11–14] in order to capture the angular dependence of interatomic forces arising due to the directional d-bonding. In section 2 we recap the ADP format and describe the methodology applied in this work for the optimization of the potential parameters. The properties predicted by the potential and their comparison with experimental data and first-principles calculations are discussed for the single-component Ni and Cr in section 3 and then for the binary Ni–Cr alloys in section 4. In the latter case, the emphasis is placed on the ability of the new potential to reproduce the binary phase diagram. The conclusions are formulated in section 5.

2. Potential format and fitting procedures

In the ADP method [3, 11-14], the total energy E of a collection of atoms is represented in the form

$$E = \frac{1}{2} \sum_{i,j(j \neq i)} \Phi_{s_i s_j}(r_{ij}) + \sum_i F_{s_i}(\bar{\rho}_i) + \frac{1}{2} \sum_{i,\alpha} (\mu_i^{\alpha})^2 + \frac{1}{2} \sum_{i,\alpha,\beta} (\lambda_i^{\alpha\beta})^2 - \frac{1}{6} \sum_i \nu_i^2, \tag{1}$$

where the indices i and j refer to atoms and the superscripts α , $\beta=1$, 2, 3 to Cartesian directions. Here, $\Phi_{s_i,s_j}(r_{ij})$ is the pair interaction potential as a function of the scalar distance r_{ij} between atoms i and j and their chemical species s_i and s_j . The function $F_{s_i}(\bar{\rho_i})$ represents the embedding energy of atom i in the host electron density $\bar{\rho_i}$ induced at site i by all other atoms. This density is given by

$$\bar{\rho_i} = \sum_{i \neq i} \rho_{s_j}(r_{ij}),\tag{2}$$

where $\rho_{s_j}(r_{ij})$ is the species-dependent electron density function assigned to atom j. The first two terms in equation (1) constitute the functional form of regular EAM potentials [15, 16] and have a central-force character. The non-central interactions are captured by the last three terms in equation (1), which depend on the local dipole vectors

$$\mu_i^{\alpha} = \sum_{i \neq i} u_{s_i s_j}(r_{ij}) r_{ij}^{\alpha},\tag{3}$$

the quadrupole tensors

$$\lambda_i^{\alpha\beta} = \sum_{i \neq i} w_{s_i s_j}(r_{ij}) r_{ij}^{\alpha} r_{ij}^{\beta},\tag{4}$$

and ν_i being the trace of $\lambda_i^{\alpha\beta}$,

$$\nu_i = \sum_{\alpha} \lambda_i^{\alpha \alpha}.$$
 (5)

These equations introduce two additional pairwise functions $u_{s_i s_j}(r)$ and $w_{s_i s_j}(r)$ in comparison with the regular EAM.

The non-central terms in equation (1) penalize the total energy for deviations of the atomic environments from cubic symmetry. While they vanish in a perfect cubic structure, they can be important in non-cubic structures and even in cubic structures under non-hydrostatic strains. They can affect the elastic constants, defect formation energies, the melting point, and many other material properties.

A complete ADP description of the binary Ni–Cr system requires 13 functions: $\Phi_{\text{NiNi}}(r)$, $\Phi_{\text{CrCr}}(r)$, $\Phi_{\text{NiCr}}(r)$, $\rho_{\text{Ni}}(r)$, $\rho_{\text{Cr}}(r)$, $F_{\text{Ni}}(\bar{\rho})$, $F_{\text{Cr}}(\bar{\rho})$, $u_{\text{NiNi}}(r)$, $u_{\text{CrCr}}(r)$, $u_{\text{NiCr}}(r)$, $u_{\text{NiCr}}(r)$, $u_{\text{NiNi}}(r)$, $u_{\text{CrCr}}(r)$ and $u_{\text{NiCr}}(r)$. Having ADP potentials for pure Ni and pure Cr, only the cross-interaction functions $\Phi_{\text{NiCr}}(r)$, $u_{\text{NiCr}}(r)$ and $u_{\text{NiCr}}(r)$ are needed to describe the binary system. All these functions were represented by analytical expressions with adjustable parameters. Specifically, the electron density functions for Ni and Cr were chosen in the form

$$\rho(r) = \psi\left(\frac{r - r_c}{h}\right) [A_0 y^{\varepsilon} e^{-\gamma y} (1 + B_0 e^{-\gamma y}) + C_0], \tag{6}$$

where $y = r - r_0$, r_c is the cutoff radius, and B_0 , C_0 , r_0 , ε , γ and h are fitting parameters. The cutoff function $\psi(x)$ is given by

$$\psi(x) = \frac{x^4}{1 + x^4} \tag{7}$$

if x < 0 and $\psi(x) \equiv 0$ if $x \geqslant 0$. The coefficient A_0 was adjusted to give a unit host electron density in the single-component crystal (fcc Ni or bcc Cr) with the equilibrium lattice parameter. For the Ni and Cr potentials, the pair interaction potentials had the form of the generalized Lennard-Jones function

$$\Phi(r) = \psi \left(\frac{r - r_c}{h}\right) \left[\frac{W_0}{b_2 - b_1} \left(\frac{b_2}{z^{b_1}} - \frac{b_1}{z^{b_2}}\right) + \delta + \xi r \right] + m\rho(r), \tag{8}$$

where $z=r/r_1$ and b_1 , b_2 , r_1 , W_0 , δ , ξ and m are fitting parameters. Mixing the functions $\rho(r)$ and $\Phi(r)$ with an adjustable weight m gives additional flexibility in optimizing the shape of $\Phi(r)$. Note that the cutoff function $\psi(x)$ guarantees that $\rho(r)$, $\Phi(r)$ and their derivatives up to the second one go smoothly to zero at the common cutoff radius r_c . For the cross-interaction potential $\Phi_{\text{NiCr}}(r)$, a more general Lennard-Jones function was used:

$$\Phi(r) = \psi \left(\frac{r - r_c}{h}\right) W_0 \left[\left(\frac{b_{12}}{r}\right)^{12} - \left(\frac{b_6}{r}\right)^6 + \left(\frac{b_{11}}{r}\right)^{11} + \dots + \frac{b_1}{r} + b_0 \right], \quad (9)$$

with the fitting parameters b_i and W_0 .

The embedding energies $F(\overline{\rho})$ of Ni and Cr were obtained by inverting the universal equation of state postulated in the form

$$E(a) = E_0 \left[1 + \alpha x + \beta \alpha^3 x^3 \frac{2x+3}{(x+1)^2} \right] e^{-\alpha x},$$
(10)

where $x = a/a_0 - 1$, $\alpha = -(9V_0B/E_0)^{1/2}$, E(a) is the energy per atom relative to a set of isolated atoms, E_0 is the equilibrium cohesive energy (minimum of E), a is the cubic lattice parameter, a_0 is the equilibrium value of a, V_0 is the equilibrium atomic volume, B is the bulk

modulus and β is a parameter. The latter controls the high-pressure behavior without changing the equilibrium lattice constant, cohesive energy or bulk modulus. The universal equation of state was initially proposed by Rose *et al* [17]. In this work, the large-separation region of E(a) was additionally modified to ensure a smooth cutoff at r_c . Note that the inversion based on equation (10) guarantees an exact fit to a_0 , E_0 and B.

Finally, the dipole and quadrupole functions were parameterized in the form

$$u(r) = \psi\left(\frac{r - r_c}{h}\right) (d_1 e^{-d_2 r} + d_3), \tag{11}$$

$$w(r) = \psi \left(\frac{r - r_c}{h}\right) (q_1 e^{-q_2 r} + q_3), \tag{12}$$

with the fitting parameters d_i and q_i .

Optimization of the cross-interactions additionally involved transformations of the potential functions. There are certain transformations that do not affect the energies of pure Ni and pure Cr but change the energies in the binary system [5, 18–23]. Such transformations are:

$$\rho_{Ni}(r) \to s_{Ni}\rho_{Ni}(r),$$
(13)

$$F_{\text{Ni}}(\bar{\rho}) \to F_{\text{Ni}}\left(\frac{\bar{\rho}}{s_{\text{Ni}}}\right),$$
 (14)

$$F_{\text{Ni}}(\bar{\rho}) \to F_{\text{Ni}}(\bar{\rho}) + g_{\text{Ni}}\bar{\rho},$$
 (15)

$$F_{\rm Cr}(\bar{\rho}) \to F_{\rm Cr}(\bar{\rho}) + g_{\rm Cr}\bar{\rho},$$
 (16)

$$\Phi_{\text{NiNi}}(r) \to \Phi_{\text{NiNi}}(r) - 2g_{\text{Ni}}\rho_{\text{Ni}}(r), \tag{17}$$

$$\Phi_{\rm CrCr}(r) \to \Phi_{\rm CrCr}(r) - 2g_{\rm Cr}\rho_{\rm Cr}(r). \tag{18}$$

The transformation coefficients $s_{\rm Ni}$, $g_{\rm Ni}$ and $g_{\rm Cr}$ were used as additional adjustable parameters. In this work we utilized a slightly modified version of an existing ADP Ni potential developed in [3]. It was noted [3] that the contribution of the non-central terms to Ni properties was relatively small. Furthermore, it was found that the quadrupole term is more effective in controlling the properties of Ni than the dipole term. Therefore, in the interest of simplicity we only included the quadrupole term in the ADP Ni potential and turned the dipole term off by setting $d_i = 0$. After this modification, the properties predicted by the Ni potential could slightly change and were thus recomputed in this paper.

For Cr, a new ADP potential was constructed. The fitting database included the experimental values of a_0 , E_0 , B, the elastic constants C_{ij} , the vacancy formation energy, and the density functional theory (DFT) surface energies γ_s for the (110) and (111) crystallographic orientations. The (100) surface orientation was fitted to the experimental value of γ_s . It additionally included the equilibrium energies of the fcc, hexagonal close packed (HCP), simple cubic and A15 structures predicted by first-principles DFT calculations. For the Ni–Cr cross-interaction functions, the database included DFT values of the equilibrium formation energies of several Ni–Cr compounds with different stoichiometries and crystal structures. The formation energy is defined as the difference between the cohesive energy of the compound per atom and the average of the cohesive energies of the atoms making up the compound. Namely, the formation energy of a compound with the Ni_nCr_m stoichiometry is

Table in optimized many parameters of the Table of potential.			
Parameter	Value	Parameter	Value
r_c (Å)	5.108 002	ε	0
h (Å)	1.955 716	$\gamma (1/\text{Å})$	9.353082×10^{-2}
W_0 (eV)	-1.342760	B_0	-6.310646
r_1 (Å)	4.168364×10^{1}	C_0	$-2.985\ 208$
b_1	2.492344×10^{-5}	r_0 (Å)	9.239768×10^{-2}
b_2	4.061 893	β	0
δ (eV)	$9.645\ 520\times 10^{-1}$	$q_1 \left(\sqrt{\text{eV}} / \text{Å}^2 \right)$	1.580879×10^3
<i>m</i> (eV)	-6.709814×10^{-1}	$q_2 (1/\text{Å})$	8.753 905
\mathcal{E} (eV Å ⁻¹)	9.745548×10^{-1}	$a_3 \left(\sqrt{\text{eV}}/\text{Å}^2\right)$	-7.143462×10^{-2}

Table 1. Optimized fitting parameters of the ADP Cr potential.

Table 2. Optimized fitting parameters of the Ni-Cr cross-interaction functions.

Parameter	Value	Parameter	Value
r_c (Å)	5.103 329	<i>b</i> ₈ (Å)	-4.15659
h (Å)	6.463 548	b_9 (Å)	-1.99229
W_0 (eV)	$7.708\ 119\times 10^{-2}$	b_{10} (Å)	-3.502440
b_0	-2.376257	b_{11} (Å)	-3.486249
b_1 (Å)	1.051441×10^{1}	b_{12} (Å)	-3.134166
b_2 (Å)	4.490 321	$q_1 \left(\sqrt{\text{eV}} / \text{Å}^2 \right)$	-2.694439×10^{2}
b_3 (Å)	-4.793837	$q_2 (1/\text{Å}^2)$	3.409711×10^2
b_4 (Å)	-4.647546	$q_3 \left(\sqrt{\text{eV}} / \text{Å} \right)$	-1.075064
b_5 (Å)	-5.016524	$s_{ m Ni}$	4.867850×10^{-1}
b_6 (Å)	2.986 347	g_{Cr}	-4.097726
<i>b</i> ₇ (Å)	4.023 827	$g_{ m Ni}$	-2.933 057

$$\frac{E(\operatorname{Ni}_{n}\operatorname{Cr}_{m})-nE_{0}(\operatorname{Ni})-mE_{0}(\operatorname{Cr})}{n+m},$$

where $E(Ni_nCr_m)$ is the energy of the compound per formula unit with the equilibrium lattice constant. The following structures were included in the fit: B1, B2, B3, $L1_0$ and $L1_1$ of NiCr, and $L1_2$, $D0_3$ and $D0_{22}$ of NiCr₃ and Ni₃Cr. All DFT values used in this works were taken from the literature [25–27].

The fitting parameters were optimized by minimizing the weighted mean-squared deviation of the computed properties from their target values using the simulated annealing method. By selecting different sets of weights, several versions of the potential were generated. Each version was tested against a set of experimental and DFT properties that were not included in the fitting database. If the tests revealed a significant flaw of the potential, it was discarded. One of the tests was the ability of the potential to predict the equilibrium lines on the Ni–Cr phase diagram as discussed below. Based on the test results, the potential showing the best performance was selected as final. Similar to the Ni case, it was found that the quadrupole terms describing the Ni–Cr interactions were sufficient and thus the dipole terms were not included ($d_i = 0$).

The optimized values of the potential parameters are listed in table 1 for Cr and table 2 for Ni–Cr. The potential functions in the effective pair format are shown in figure 1.

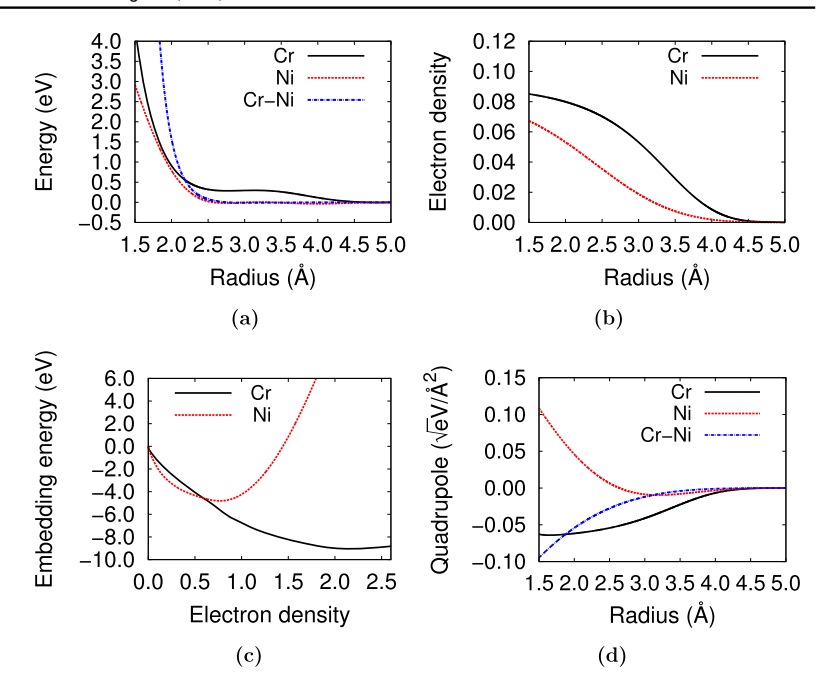


Figure 1. ADP potential functions. (a) Pair interaction. (b) Electron density. (c) Embedding energy. (d) Quadrupole function.

3. Testing of the Ni and Cr potentials

Tables 3 and 4 compare predictions of the ADP Ni and Cr potentials with experimental and DFT data for a set of properties that are most relevant to atomistic simulations. The tables also include predictions of the EAM Ni [22] and EAM Cr [6, 7] potentials from the literature. Most of the DFT Ni properties from the literature refer to the ferromagnetic state unless otherwise is indicated. All defect energies reported in the tables were obtained by static relaxation at 0 K temperature. The vacancy migration energy E_{ν}^{m} was computed by the nudged elastic band method [28, 29]. The energy along the reaction coordinate of the vacancy jump was found to have a single maximum at the midpoint (1/2)[110] for Ni and (1/2)[111] for Cr. The interstitial formation energies were computed for several split dumbbell configurations with different orientations. The energies of the alternate crystal structures were minimized with respect to the lattice parameter and reported relative to the ground-state structure. All calculations utilized the open source molecular dynamics (MD) code LAMMPS [30].

The ADP Ni potential demonstrates moderate improvements over the EAM version [22] with respect to the vacancy formation and migration energies, surface energies, and the energies of the non-centrosymmetric HCP and DC structures (table 3). For Cr, the ADP potential accurately reproduces the experimental cohesive energy, lattice parameter, elastic constants of the paramagnetic phase, and the vacancy formation energy E_{ν}^{f} (table 4). It slightly underestimates the vacancy migration barrier E_{ν}^{m} and systematically underestimates the interstitial formation energies and the surface energies. However, the rankings of the different interstitial configurations and surface orientations are predicted correctly. During the

Table 3. Properties of Ni calculated with the ADP (this work) and EAM [22] potentials in comparison with experimental data and first-principles DFT calculations. The potential was fitted to the experimental properties marked by an asterisk. The references to the experimental and some of the DFT data can be found in [3, 22].

	Experiment ^{a,b}	DFT	EAM ^b	ADP
$a_0 (\mathring{A})^*$	3.52	3.52°	3.52	3.52
$B (GPa)^*$	181.0	186 ^c ; 185.9 ^d	181.0	181.0
$E_0 (eV)^*$	-4.45		-4.45	-4.45
$C_{11} (\text{GPa})^*$	246.5	287°; 276°	241.3	241.3
$C_{12} (\text{GPa})^*$	147.3	155°; 159°	150.8	150.8
$C_{44} \text{ (GPa)}^*$	124.7	150°; 132°	127.3	127.3
$E_{\nu}^{f} (eV)^{*}$	1.60	1.65 ^f ; 1.44 ^d	1.57	1.60
$E_{\nu}^{m} (eV)^{*}$	1.30	1.09 ^f	1.19	1.33
Melting point (K)	1728		1701	1772
γ_s (J m ⁻²):				
{100}	2.28 ^g	2.21 ^e	1.94	1.96
{110}*	2.28 ^g	2.29 ^e	2.09	2.10
{111}	2.28 ^g	1.92 ^e	1.76	1.76
Alternate crystal str	ructures:			
Structure			EAM ^b	ADP
HCP (eV/atom)*		$0.03^{a,b}; 0.010^{h}$	0.02	0.02
bcc (eV/atom)*		$0.11^{a,b}$; 0.091^{h} ; 0.098^{e}	0.07	0.07
$L1_2 \text{ (eV/atom)}^*$		$0.66^{a,b}$	0.54	0.56
SC (eV/atom)*		$1.00^{a,b}$; 0.796^e	0.72	0.72
DC (eV/atom)*		1.94 ^{a,b} ; 1.197 ^h	1.42	1.56

^a [3, 22] and references therein.

potential development, some versions of the potential gave higher interstitial and surface energies, but they tended to overestimate the melting temperature. We thus selected a version that was considered a reasonable compromise.

Overall, with respect to the properties mentioned above, the ADP Cr potential performs at about the same level of accuracy as the EAM potential from [7] and both are more accurate than the EAM potential from [6]. It should be emphasized, however, that by contrast to the EAM potentials [6, 7], the ADP potential was additionally fitted to three surface energies and DFT energies of four alternate crystal structures of Cr. This expansion of the fitting database improved the transferability of the potential to a wider range of configurations. At the same time, this limited its ability to improve certain properties, such as the interstitial formation energies. Table 4 shows that the fit to the alternate structural energies is reasonably good, except for the fcc energy which is too small. We were unable to achieve a better agreement for the fcc energy without compromising the accuracy of other properties.

The phonon dispersion curves for Ni and Cr were computed by MD simulations at 293 K. The method [31] reconstructs the dynamical matrix of the crystal from correlations

b [3, 22] and references therein.

^c [47].

^d [49].

^e Materials project [27] (non-magnetic).

f [48].

^g Average crystal orientation.

^h [26].

Table 4. Properties of Cr calculated with the ADP potential (this work) in comparison with experimental, DFT and EAM data. Properties included in the fitting of the ADP potential are marked by an asterisk. $E_{\langle 100 \rangle}^f$, $E_{\langle 110 \rangle}^f$, $E_{\langle 111 \rangle}^f$, E_O^f and, E_T^f are the interstitial formation energies for the $\langle 100 \rangle$, $\langle 110 \rangle$ and $\langle 111 \rangle$ -oriented dumbbell configurations, and octahedral and tetrahedral configurations, respectively.

	Experiment	DFT	EAM ^{a,b}	ADP	
$a_0 (\mathring{A})^*$	2.878°; 2.88 ^d	2.834° 2.87 ^d	2.87 ^a ; 2.875 ^b	2.88	
$B (GPa)^*$	208°	226.20°; 236.80°	148 ^a ; 207 ^b	210	
$E_0 (eV)^*$	-4.10^{c}		$-4.10^{\mathrm{a}}; -4.10^{\mathrm{b}}$	-4.10	
$C_{11} (\text{GPa})^*$	410.7°	445.6°; 460.60°	204.7 ^a ; 411 ^b	413.81	
$C_{12} (\text{GPa})^*$	106.7°	116.5°; 124.90°	119.7 ^a ; 105 ^b	108.09	
$C_{44} (\text{GPa})^*$	105°	101.20°; 103.8°	84.5 ^a ; 105 ^b	105.16	
E_{v}^{f} (eV)*	2.0°	2.59°; 2.64°	1.09 ^a ; 2.14 ^b	1.81	
E_{v}^{m} (eV)	0.95°	0.91 ^e		0.83	
$E_{\langle 100 \rangle}^f$ (eV)		6.78°; 6.64°		4.02	
$E_{\langle 110 \rangle}^f$ (eV)		5.66 ^c ; 5.68 ^e	3.03 ^a ; 5.16 ^b	3.99	
$E_{\langle 111 \rangle}^f$ (eV)		5.68°; 5.66°	2.84 ^a ; 5.78 ^b	3.85	
E_O^f (eV)		6.72 ^e		4.09	
E_T^f (eV)		6.19 ^e		4.04	
Melting point (K)	2136 ^f			2168	
γ_s (J m ⁻²):					
{100}*	2.30 ^d	3.979 ^g ;		2.33	
{110}*		3.1 ^d ; 3.505 ^g		2.20	
{111}*		4.123 ^g		2.46	
Alternate crystal structures:					
Structure		DFT	EAM	ADP	
A15 (eV/atom)*		0.065 ^h ; 0.066 ⁱ		0.15	
fcc (eV/atom)*		0.389 ^h ; 0.383 ⁱ	0.025 ^b	0.09	
HCP (eV/atom)*		0.447 ^h ; 0.392 ⁱ		0.38	
SC (eV/atom)*		1.019 ^h		0.81	

^a [6].

between atomic displacements during an MD run. Fourier transformation of the dynamical matrix permits calculations of the phonon frequencies along high-symmetry directions in the reciprocal space. Figure 2 compares the results predicted by the potentials with experimental dispersion curves measured by neutron scattering at the same temperature [32, 33]. While most of the low phonon frequencies are reproduced accurately, the frequencies of zoneboundary phonons tend to be overestimated (Ni) or underestimated (Cr) by approximately 10%. For Cr, there is also a significant discrepancy along the H-P direction on the zone

^b [6].

^c [50, 52].

^d [51].

e [54].

f [55].

^g [53].

^h [24].

i Materials project [27].

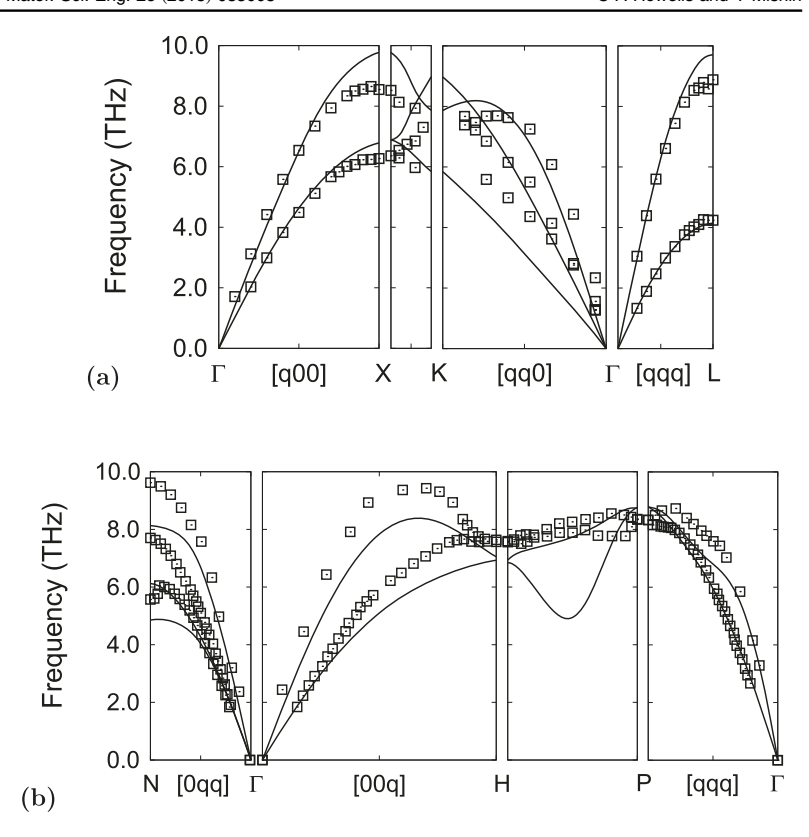


Figure 2. Phonon dispersion relations of (a) Ni and (b) Cr predicted by the ADP potentials (solid lines) in comparison with experimental data (points) [32, 33].

surface. Overall, given that phonon frequencies were not included in the fitting database, we consider the obtained agreement with experiment quite satisfactory.

Linear thermal expansion of Ni and Cr was evaluated by NPT Monte Carlo simulations using a cubic periodic block with 2048 atoms for Ni and 2000 atoms for Cr. The results predicted by the potentials are plotted in figure 3 in comparison with experimental data [34]. The plots show the relative expansion $(a(T) - a_{RT})/a_{RT} \cdot 100\%$, where a_{RT} is the cubic lattice parameter at room temperature (293 K). Each curve ends near the experimental melting point. The agreement with experiment is generally good, especially considering that thermal expansion was not included in the potential fits. In fact, the agreement remains very good up to 600 K for Ni and about 1200 K for Cr. At higher temperatures, the potentials under-predict (Ni) or over-predict (Cr) the experimental data.

The melting temperatures of Ni and Cr were computed by the phase coexistence method [35, 36]. For each metal, a periodic simulation block was prepared that contained approximately cubic volumes of the stress-free solid and liquid phases separated by a (100)-oriented interface. The block contained 24 000 atoms (12.7 nm dimension normal to the interface) for Ni and 12 240 atoms (respectively, 8.8 nm) for Cr. The initial temperature was chosen to be close to the expected melting point. The cross-section of the simulation block (parallel to the interface) was fixed, while the dimension normal to the interface was allowed to vary. Next, a

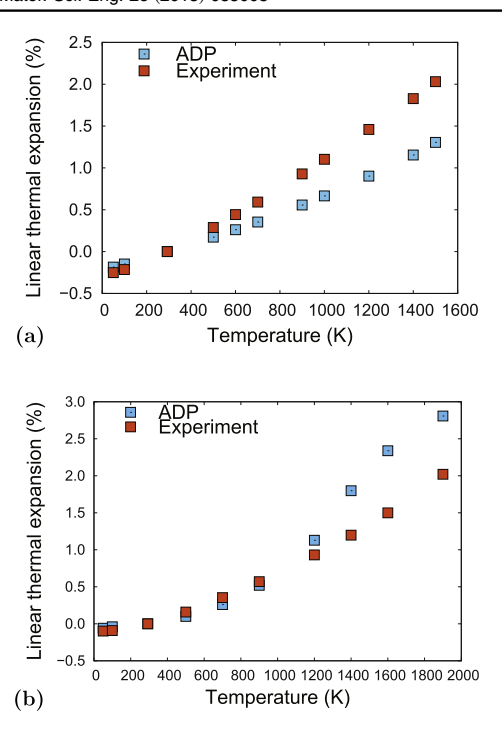


Figure 3. Linear thermal expansion relative to room temperature (293 K) calculated with the ADP potentials for (a) Ni and (b) Cr in comparison with experimental data [34].

long NPH (constant enthalpy) MD simulation was executed at the pressure of 1 atm applied normal to the interface. During the simulation, partial melting or solidification of the material occurred accompanied by a change in temperature. This change eventually stopped when the conditions of solid–liquid phase equilibrium were met. Accordingly, the temperature reached a value T_m corresponding to the melting point of the metal at the ambient pressure. The melting temperatures obtained are listed in tables 3 and 4. For Ni, T_m exceeds the experimental value by 44 K (2.5%), while T_m of Cr underestimates the experiment by 32 K (1.5%). Given that neither T_m nor any liquid properties were in the fitting database, this agreement is evidence of good transferability of the potentials to high-temperature properties.

4. Testing of the binary Ni-Cr potential

Table 5 compares the DFT formation energies of several binary Ni–Cr compounds with formation energies computed with the ADP potential. The DFT energies from the OQMD database [26] were fitted during the development of the potential while the DFT energies from the AFLOW database [25] are included for comparison. While the agreement of the DFT energies with the potential predictions are far from perfect, there is obviously a strong correlation across a 1.8eV wide energy range as illustrated in figure 4.

As the main test of the Ni-Cr potential we focused on its ability to predict the Ni-Cr phase diagram. The Ni-Cr phase diagram is eutectic type containing fcc and bcc-based solid solutions and a liquid phase. The diagram was calculated by a method similar to the one

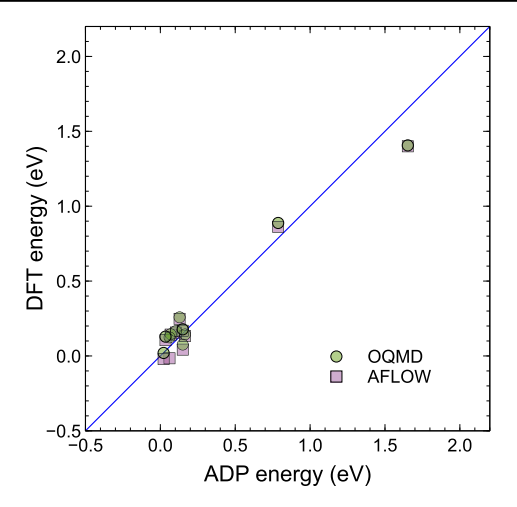


Figure 4. DFT formation energies of Ni–Cr compounds plotted against the formation energies predicted by the ADP potential. The line of perfect agreement is shown as a guide to the eye.

Table 5. Formation energies (eV/atom) of different structures of Cr–Ni calculated with the ADP potential in comparison with DFT data. The DFT energies from the OQMD database [26] were used in the fitting process while the energies from AFLOW [25, 56] are included to show the scatter of the DFT calculations.

Structure	DFT (NiCr)	ADP (NiCr)
B1	0.888 0 ^a ; 0.862 2 ^b	0.786 7
B2	$0.258 0^{\rm a}; 0.248 0^{\rm b}$	0.128 5
B3	1.406 0 ^a ; 1.399 8 ^b	1.652 4
$L1_0$	0.076 0 ^a ; 0.042 2 ^b	0.149 6
$L1_1$	$0.145 0^{a}; 0.142 6^{b}$	0.068 7
Structure	DFT (NiCr ₃)	ADP (NiCr ₃)
$\overline{L1_2}$	0.144 0 ^a ; 0.133 2 ^b	0.164 6
$D0_3$	0.166 0 ^a ; 0.156 4 ^b	0.103 8
$D0_{22}$	$0.178 0^{a}; 0.168 3^{b}$	0.149 3
Structure	DFT (Ni ₃ Cr)	ADP (Ni ₃ Cr)
$\overline{L1_2}$	$0.124~0^{\rm a};~-0.015~6^{\rm b}$	0.061 2
$D0_3$	0.129 0 ^a ; 0.105 3 ^b	0.034 4
$D0_{22}$	$0.020 0^{a}; -0.020 8^{b}$	0.021 8

^a [26].

developed previously for the Cu-Ag system [37] with some computational improvements. The solid-solid equilibrium lines were computed by thermodynamic integration while the solid-liquid equilibrium lines were obtained by direct phase coexistence simulations.

In the thermodynamic integration method, the first step was to obtain the Gibbs free energies, g_0 , of pure Cr and Ni at a reference temperature T_0 using the quasi-harmonic

^b [25, 56].

approximation as in the previous work [37–41]. In this approximation, the classical harmonic free energy is added to the potential energy of the system and the total free energy is minimized at the chosen reference temperature. The same reference temperature $T_0 = 293 \, \mathrm{K}$ was chosen for both Cr and Ni. Next, NPT Monte Carlo simulations at zero pressure were executed for each metal for a set of temperatures T ranging from T_0 to temperatures above the expected eutectic point. At each temperature, the average potential energy per atom was computed and the total energy per atom was obtained by adding the classical kinetic energy $3k_{\mathrm{B}}T/2$, k_{B} being the Boltzmann factor. Because the pressure was zero, this total energy could be equated to the enthalpy per atom h(T). The latter was approximated by a quadratic function

$$h(t) = h_0 + AT + BT^2, (19)$$

with fitting parameters h_0 , A and B. The Gibbs free energy of the metal, g(T), was then determined by integrating the Gibbs–Helmholtz equation $\partial (g/T)/\partial T = -h/T^2$ between the reference temperature T_0 and a chosen temperature $T > T_0$, giving the analytical expression

$$g(T) = g_0 \frac{T}{T_0} + h_0 \left(1 - \frac{T}{T_0} \right) - BT(T - T_0) - AT \ln \left(\frac{T}{T_0} \right). \tag{20}$$

This calculation resulted in free energy functions $g_{Ni}(T)$ and $g_{Cr}(T)$.

Next, the semi-grand canonical Monte Carlo method was applied, in which the total number of atoms in the simulation block and the chemical potential difference, $\Delta\mu=\mu_{\rm Cr}-\mu_{\rm Ni}$, were fixed, while the chemical species of the atoms were allowed to switch randomly between Ni and Cr. In addition, individual atoms were subject to small random displacements and all three dimensions of the simulation block were allowed to fluctuate to ensure the zero-pressure condition along each Cartesian direction. The computations employed a cubic periodic supercell containing N=4000 atoms, with the initial state being elemental fcc Ni or elemental bcc Cr. For each temperature and $\Delta\mu$ value, the system was equilibrated by 70 000 Monte Carlo steps (each step being a cycle of N attempted moves), after which the equilibrium alloy composition was obtained by averaging over 40 000 additional Monte Carlo steps. The alloy composition c was defined as the fraction of Cr atoms. Te simulations utilized the parallel Monte Carlo code ParaGrandMC [42]. As a result, $\Delta\mu(c,T)$ functions were obtained for a set of temperatures for the fcc and bcc-based solid solutions. At each temperature, these functions were fitted by the analytical expression

$$\Delta\mu(c, T) = g_{\text{Ni}}(T) - g_{\text{Cr}}(T) - \alpha - \beta c - \gamma c^2 - k_{\text{B}}T \ln\left(\frac{c}{1 - c}\right)$$

with the fitting parameters α , β and γ . Knowing these parameters, the Gibbs free energy function

$$g(c, T) = g_{Cr}(T)c + g_{Ni}(T)(1 - c) + \alpha c + \frac{\beta}{2}c^2 + \frac{\gamma}{3}c^3 + k_B T[c \ln(c) + (1 - c)\ln(1 - c)]$$
(21)

was reconstructed for each solid solution, see example in figure 5. Finally, the equilibrium compositions of the phases were computed by constructing a common tangent to the free energy functions by a numerical procedure (figure 6). Repeating this calculation for several temperatures, the solvus lines bounding the miscibility gap on the phase diagram were obtained.

To compute the solidus and liquidus lines, the same solid-liquid simulation block was utilized as for the melting point calculations in pure Ni and Cr (section 3). Instead of MD,

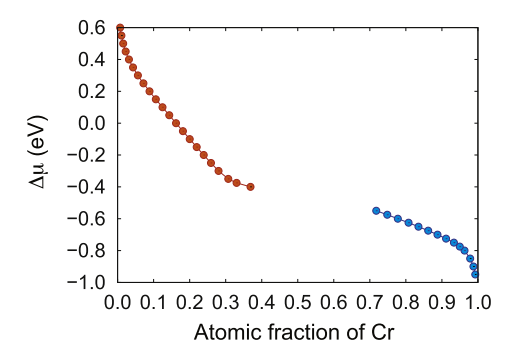


Figure 5. Example of the chemical potential difference versus alloy composition at T = 1325 K. The left and right branches represent the Ni-based and Cr-based solid solutions, respectively.

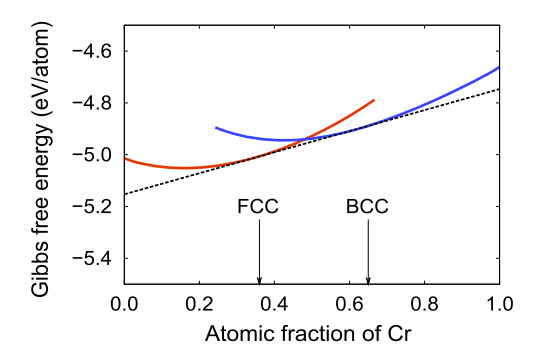


Figure 6. Common tangent construction (dashed line) for computing the equilibrium phase compositions at T=1325 K. The left (red) and right (red) curves represent the Ni-based and Cr-based solid solutions, respectively. Their equilibrium chemical compositions are marked by the arrows labeled fcc and bcc.

semi-grand canonical Monte Carlo simulations were implemented in the composition-controlled mode using the same methodology as described above. At each temperature, the imposed average chemical composition of the system was adjusted so that equilibrium would be reached with about half of the block being liquid and the other half solid. After equilibration, the chemical compositions of the phases were computed by averaging over 80 000 Monte Carlo steps using bulk regions unaffected by the solid–liquid interface.

Figure 7 compares the phase diagram predicted by the ADP potential with the experimental phase diagram known from the literature [43]. The computed phase diagram is topologically correct and even predicts the eutectic temperature in agreement with experiment, although the eutectic composition is somewhat shifted towards the Ni side. Overall, the agreement with the experimental phase diagram is good.

For a more detailed comparison with experiment, the lattice parameters of the phases were computed for several alloy composition by semi-grand canonical NPT simulations at several temperatures and the results were plotted together with the respective experimental x-ray diffraction measurements. Examples are shown in figure 8. For the Cr-based solution, the measurements were made at high temperatures to keep the samples in the single-phase

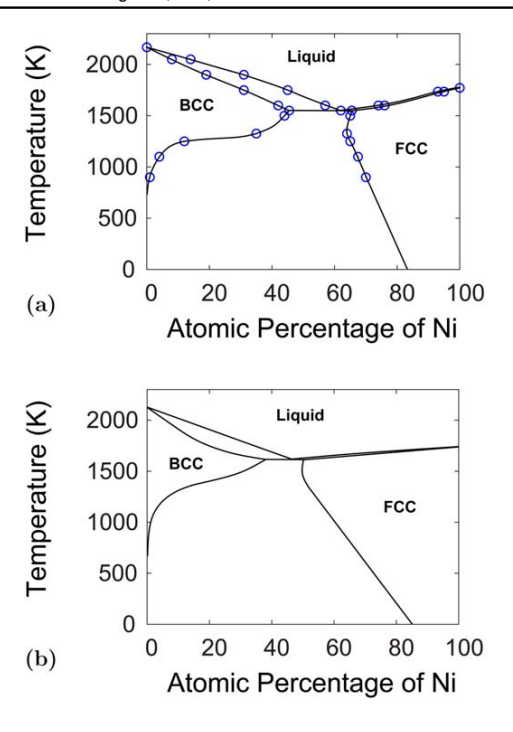


Figure 7. Ni–Cr phase diagram predicted by the ADP potential (a) in comparison with experiment [43] (b).

state (see the phase diagram in figure 7). By contrast, the Ni-based solution has a wider homogeneity range and the measurements could be made at lower temperatures. In both cases, the ADP potential performs quite well. There is a slight shift in the absolute values of the lattice parameter, but the slope of the temperature dependence is reproduced accurately without fitting.

Figure 9 shows the ADP formation enthalpy of the Ni-based solid solutions as a function of chemical composition at the temperature of 1550 K. Zero-pressure Monte Carlo simulations were applied using a cubic periodic block containing 4000 atoms. The methodology was similar to the one applied for phase diagram calculations (section 4) with the energy averaged over 65 000 Monte Carlo steps after equilibration. The formation enthalpy H_f of a Cr_xNi_{1-x} solid solution was defined as

$$H_f = H - xH_{\rm Cr} - (1 - x)H_{\rm Ni},$$
 (22)

where x is the fractional composition of Cr, $H_{\rm Cr}$ and $H_{\rm Ni}$ are the enthalpies of pure bcc Cr and fcc Ni, respectively, and H is the enthalpy of the binary solution. The plot displays a local minimum at about 20%Cr with a negative formation enthalpy, indicating an ordering tendency. For comparison, figure 9 includes two sets of experimental data [2, 44] measured by calorimetry. The experiment also shows a local minimum, although it is shallower and shifted to about 10%Cr. Despite this discrepancy, the ADP potential does capture the essential trend.

Finally, figure 10 shows a similar comparison for the Gibbs formation energy defined by a formula similar to equation (22). The experimental measurements [2] were made at 1550 K

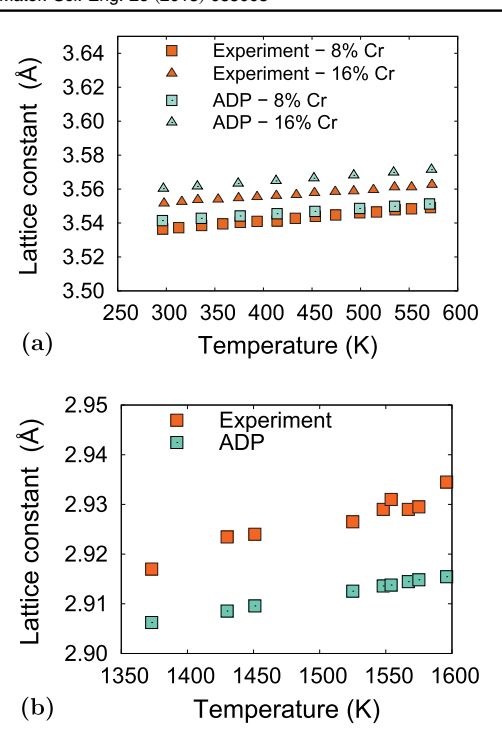


Figure 8. (a) Lattice constant as a function of temperature for two Ni-based fcc alloys in comparison with experiment [57]. (b) Same for Cr-30%Ni alloy in comparison with experiment [58].

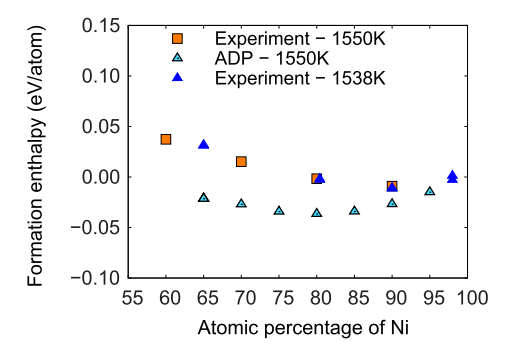


Figure 9. ADP formation enthalpy of the fcc-based Cr–Ni phase as a function of chemical composition at the temperature of 1550 K. Experimental measurements at 1550 K [2] and 1538 K [44] are shown for comparison.

(just below the eutectic) and cover the composition domains of both phases at this temperature. Since the ADP-predicted eutectic temperature is somewhat lower, the temperature of 1500 K was chosen for the calculations. The Gibbs energies of the phases were computed as part of the phase diagram calculations discussed in section 4. The ADP predictions slightly over-bind both phases, but otherwise the comparison is quite favorable, especially

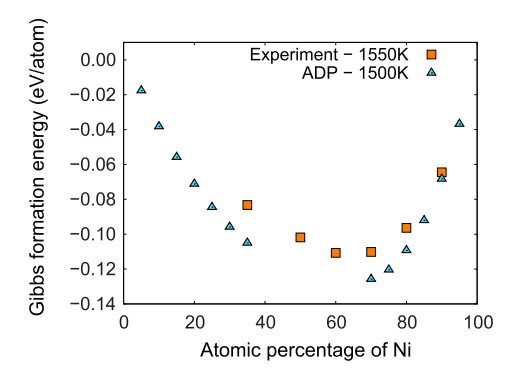


Figure 10. Gibbs formation energy of the Ni-based and Cr-based phases as a function of chemical composition. The ADP predictions at 1500 K are compared with experimental measurements [2] at 1550 K.

considering that high-temperature properties of the phases were not part of the potential development.

5. Conclusions and outlook

The ADP Ni–Cr potential developed in this work demonstrates a reasonable agreement with the available DFT and experimental data for a large set of properties of both elements as well as their alloys. Given that Cr is a bcc transition metal, the ADP format chosen in this paper appears to be more appropriate than the regular EAM format used for the Ni–Cr system in the previous work [9].

The fact that the potential reproduces the experimental Ni–Cr phase diagram without a direct fit points to its good transferability to high-temperature properties over the entire compositional range. Since the potential correctly predicts the solidus and liquidus lines on the phase diagram, it might be suitable for simulations of the melting and solidification processes. In particular, the free energies and mobilities of the solid—liquid interfaces could be computed and utilized as input material parameters needed for continuum modeling of such processes. This type of modeling is especially relevant to the additive manufacturing of Inconel alloys [45] using Ni–Cr as a simple prototype.

Moreover, since the potential predicts the solvus lines in agreement with experiment, it can be suitable for simulations involving thermodynamic coexistence of the Ni-based and Cr-based phases of this system. For example, this opens an opportunity to study the structure and properties of fcc—bcc interfaces as a function of temperature (and thus the bulk phase compositions) and bicrystallography. In particular, dislocation transmission through such interfaces could be investigated in the context of precipitation hardening and creep deformation.

Finally, the development of the Ni–Cr potential in this work could be considered as the first step towards ternary Fe–Ni–Cr and Ni–Al–Cr systems as models of austenitic steels and Ni-based superalloys, respectively. These systems, in turn, could serve as starting points for the modeling of multicomponent concentrated solid solution alloys, where Cr can play a particularly important role, see for example [46].

Acknowledgments

This work was supported by the National Science Foundation, Division of Materials Research, under Award No. 1708314.

ORCID iDs

Y Mishin https://orcid.org/0000-0001-7299-433X

References

- [1] Massalski T B (ed) 1986 Binary Alloy Phase Diagrams (Materials Park, OH: ASM)
- [2] Hultgren R, Desai P D, Hawkins D T, Gleiser M and Kelley K K (ed) 1973 Selected Values of the Thermodynamics Properties of Binary Alloys (Metals Park, OH: ASM)
- [3] Mishin Y, Mehl M J and Papaconstantopoulos D A 2005 Phase stability in the Fe-Ni system: investigation by first-principles calculations and atomistic simulations Acta Mater. 53 4029-41
- [4] Mishin Y, Farkas D, Mehl M J and Papaconstantopoulos D A 1999 Interatomic potentials for monoatomic metals from experimental data and ab initio calculations Phys. Rev. B 59 3393–407
- [5] Purja Pun G P and Mishin Y 2009 Development of an interatomic potential for the Ni–Al system Phil. Mag. 89 3245–67
- [6] Farkas D, Schon C G, De Lima M S F and Goldenstein H 1996 Embedded atom computer simulation of lattice distortion and dislocation core structure and mobility in Fe–Cr alloys Acta Mater. 44 409–19
- [7] Wallenius J, Olsson P, Lagerstedt C, Sandberg N, Chakarova R and Pontikis V 2004 Modeling of chromium precipitation in Fe–Cr alloys Phys. Rev. B 69 094103
- [8] Bangwei Z, Yifang O, Shuzhi L and Zhanpeng J 1999 An analytic MEAM model for all BCC transition metals *Physica* B 262 218–25
- [9] Bonny G, Castin N and Terentyev D 2013 Interatomic potential for studying ageing under irradiation in stainless steels: the FeNiCr model alloy *Modelling Simul. Mater. Sci. Eng.* 21 085004
- [10] Bonny G, Chakraborty D, Padley S, Manzoor A, Castin N, Phillpot S R and Aidhy D S 2018 Classical interatomic potential for quaternary Ni–Fe–Cr–Pd solid solution alloys *Modelling Simul. Mater. Sci. Eng.* 26 065014
- [11] Mishin Y and Lozovoi A Y 2006 Angular-dependent interatomic potential for tantalum Acta Mater. 54 5013–26
- [12] Hashibon A, Lozovoi A Y, Mishin Y, Elsässer C and Gumbsch P 2008 Interatomic potential for the Cu-Ta system and its application to surface wetting and dewetting *Phys. Rev.* B 77 094131
- [13] Apostol F and Mishin Y 2010 Angular-dependent interatomic potential for the aluminumhydrogen system Phys. Rev. B 82 144115
- [14] Purja Pun G P, Darling K A, Kecskes L J and Mishin Y 2015 Angular-dependent interatomic potential for the Cu-Ta system and its application to structural stability of nano-crystalline alloys Acta Mater. 100 377-91
- [15] Daw M S and Baskes M I 1983 Semiempirical, quantum mechanical calculation of hydrogen embrittlement in metals *Phys. Rev. Lett.* 50 1285–8
- [16] Daw M S and Baskes M I 1984 Embedded-atom method: derivation and application to impurities, surfaces, and other defects in metals *Phys. Rev.* B 29 6443–53
- [17] Rose J H, Smith J R, Guinea F and Ferrante J 1984 universal features of the equation of state of metals *Phys. Rev.* B 29 2963–9
- [18] Daw M S 1989 Embedded-atom method: many-body description of metallic cohesion Atomistic Simulation of Materials: Beyond Pair Potentials ed V Vitek and D J Srolovitz (New York: Plenum) pp 181–91
- [19] Johnson R A 1989 Alloy models with the embedded-atom method Phys. Rev. B 39 12554
- [20] Voter A F 1994 Intermetallic Compounds ed J H Westbrook and R L Fleischer vol 1 (New York: Wiley) p 77

- [21] Mishin Y 2005 Interatomic potentials for metals *Handbook of Materials Modeling* ed S Yip (Dordrecht: Springer) ch 2.2 pp 459–78
- [22] Mishin Y 2004 Atomistic modeling of the γ and γ' phases of the Ni–Al system *Acta Mater.* 52 1451–67
- [23] Bonny G and Pasianot R C 2010 Gauge transformations to combine multi-component many-body interatomic potentials *Phil. Mag. Lett.* 90 559–63
- [24] Lin Y S, Mrovec M and Vitek V 2014 A new method for development of bond-order potentials for transition bcc metals *Modelling Simul. Mater. Sci. Eng.* 22 034002
- [25] Curtarolo S et al 2012 AFLOWLIB.ORG: A distributed materials properties repository from highthroughput ab initio calculations Comput. Mater. Sci. 58 227–35
- [26] Saal J E, Kirklin S, Aykol M, Meredig B and Wolverton C 2013 Materials design and discovery with high-throughput density functional theory: the open quantum materials database (OQMD) JOM 65 1501
- [27] Jain A et al 2013 The materials project: a materials genome approach to accelerating materials innovation APL Mater. 1 011002
- [28] Jónsson H, Mills G and Jacobsen K W 1998 Nudged elastic band method for finding minimum energy paths of transitions Classical and Quantum Dynamics in Condensed Phase Simulations ed B J Berne et al (Singapore: World Scientific) p 1
- [29] Henkelman G and Jonsson H 2000 Improved tangent estimate in the nudged elastic band method for finding minimum energy paths and saddle points J. Chem. Phys. 113 9978–85
- [30] Plimpton S 1995 Fast parallel algorithms for short-range molecular-dynamics J. Comput. Phys. 117 1–19
- [31] Kong L T 2011 Phonon dispersion measured directly from molecular dynamics simulations Comput. Phys. Comm. 182 2201–7
- [32] Birgenau R J, Cordes J, Dolling G and Woods A D B 1964 Normal modes of vibration of nickel Phys. Rev. A 136 1359–65
- [33] Shaw W M and Muhlestein L D 1971 Investigation of the phonon dispersion relations of chromium by inelastic neutron scattering *Phys. Rev.* B 4 969–73
- [34] Touloukian Y S, Kirby R K, Taylor R E and Desai P D (ed) 1975 Thermal Expansion: Metallic Elements and Alloys vol 12 (New York: Plenum) (https://doi.org/10.1007/978-1-4757-1622-1)
- [35] Morris J, Wang C, Ho K and Chan C 1994 Melting line of aluminum from simulations of coexisting phases *Phys. Rev.* B 49 3109–15
- [36] Morris J and Song X 2002 The melting lines of model systems calculated from coexistence simulations J. Chem. Phys. 116 9352–8
- [37] Williams P L, Mishin Y and Hamilton J C 2006 An embedded-atom potential for the Cu-Ag system Modelling Simul. Mater. Sci. Eng. 14 817-33
- [38] Foiles S M 1994 Evaluation of harmonic methods for calculating the free energy of defects in solids Phys. Rev. B 49 14930–8
- [39] Frolov T and Mishin Y 2009 Temperature dependence of the surface free energy and surface stress: an atomistic calculation for cu(110) Phys. Rev. B 79 45430–40
- [40] Mishin Y 2014 Calculation of the γ/γ' interface free energy in the Ni–Al system by the capillary fluctuation method *Modeling Simul. Mater. Sci. Eng.* 22 045001
- [41] Hickman J and Mishin Y 2016 Disjoining potential and grain boundary premelting in binary alloys Phys. Rev. B 93 224108
- [42] Yamakov V The ParaGrandMC code can be obtained from the NASA Software Catalog https://software.nasa.gov/software/LAR-18773-1
- [43] Okamoto H, Schlesinger M E and Mueller E M (ed) 1992 ASM Handbook 3: Alloy Phase Diagrams vol 3 (Materials Park, OH: ASM International)
- [44] Dench W A 1963 Adiabatic high-temperature calorimeter for the measurement of heats of alloying Trans. Faraday Soc. 59 1279–92
- [45] Tucho W M, Cuvillier P, Sjolyst-Kverneland A and Hansen V 2017 Microstructure and hardness studies of Inconel 718 manufactured by selective laser melting before and after solution heat treatment *Mater. Sci. Eng.* A 689 220–32
- [46] Wu Z, Troparevsky M, Gao Y F, Morris J R, Stocks G M and Bei H 2017 Phase stability, physical properties and strengthening mechanisms of concentrated solid solution alloys *Current Opin.* Solid State Mater. Sci. 21 267–84

- [47] Guo G Y and Wang H H 2000 Gradient-corrected density functional calculation of elastic constants of Fe, Co and Ni in bcc, fcc and hcp structures Chin. J. Phys. 38 949–61
- [48] Tucker J D, Najafabadi R, Allen T R and Morgan D 2010 *Ab initio*-based diffusion theory and tracer diffusion in Ni-Cr and Ni-Fe alloys *J. Nucl. Mater.* **405** 216–34
- [49] Nazarov R, Hickel T and Neugebauer J 2012 Vacancy formation energies in fcc metals: Influence of exchange-correlation functionals and correction schemes *Phys. Rev.* B 85 144118
- [50] Olsson P, Wallenius J, Domain C, Nordlund K and Malerba L 2005 Two-band model of alphaprime phase formation in Fe-Cr Phys. Rev. B 72 214119
- [51] Punkkinen M P J, Hu Q M, Kwon S, Johansson B, Kollar J and Vitos L 2011 Surface properties of 3d transition metals *Phil. Mag.* 91 3627–40
- [52] Campbell J L and Schulte C W 1979 Positron trapping and self-diffusion activation energies in chromium Appl. Phys. 19 149–52
- [53] Vitos L, Ruban A V, Skriver H L and Kollár J 1998 The surface energy of metals Surf. Sci. 411 186–202
- [54] Dudarev S 2013 Density functional theory models for radiation damage Annu. Rev. Mater. Res. 43 35–61
- [55] Xiong W, Selleby M, Chen Q, Odquist J and Du Y 2010 Phase equilibria and thermodynamic properties in the Fe-Cr system Crit. Rev. Solid State Mater. Sci. 35 125-52
- [56] Curtarolo S et al 2012 AFLOW: an automatic framework for high-throughput materials discovery Comput. Mater. Sci. 58 218–26
- [57] Pavlovic A S, Babu V S and Seehra M S 1996 High-temperature thermal expansion of binary alloys of Ni with Cr, Mo and Re: a comparison with molecular dynamics simulations J. Phys.: Condens. Matter. 8 3139–950
- [58] Wyder W C and Hoch M 1963 The polymorphic forms of chromium. examination of the Cr–Ni and Cr–Fe systems by high-temperature x-ray diffraction technique *Trans. Metall. Soc. AIME* 227 588–92